Korean J. Chem. Eng., 39(9), 2505-2512 (2022)
DOI: 10.1007/s11814-021-1024-9

pISSN: 0256-1115
eISSN: 1975-7220

Powder X-ray diffraction analysis of Cu/Cu_2O nanocomposites synthesized by colloidal solution method

Nguyen Hoang Lam, Nam Le, Eui Seon Kim, Mohaseen Salim Tamboli, Asiya Mohaseen Tamboli, Nguyen Tam Nguyen Truong† and Jae Hak Jung†

School of Chemical Engineering, Yeungnam University, 280 Daehak-ro, Gyeongsan 38541, Korea
(*Received 13 September 2021 • Revised 9 November 2021 • Accepted 23 November 2021*)

Abstract−Cu/Cu_2O powder nanocomposites (PNCs) were successfully synthesized by colloidal solution method. To investigate the influence of oxidant agent concentration on the crystallite size and lattice constant of the PNCs, X-ray diffraction (XRD) was utilized to collect the database for crystal growth analysis. Due to the imperfect crystal growth, the Nelson-Riley function and the Williamson-Hall method were used to confirm the precise values of the PNCs. The Rietveld refinement method based on the XRD pattern was used. The XRD results show that the diffraction peaks were mainly assigned to the cubic structure, in good agreement with the ICDD standards. Furthermore, the change in oxidant agent concentration led to a very small change of microstrain in the peaks of Cu/Cu_2O PNCs. Using these methods can aid in the precise study of the crystalline structure of the material, which can then be calculated to adjust the influencing conditions during the synthesis of the material.

Keywords: Crystallite Size, Cu/Cu_2O Nanocomposite, Lattice Strain, Rietveld Refinement, X-ray Diffraction

INTRODUCTION

There have been many reports for the development of size and shape controllable nanoparticles due to their selective size, morphology and crystal structure. Various nanoparticles, such as titanium dioxide (TiO_2), tin dioxide (SnO_2), and zinc oxide (ZnO), have been shown to be good candidates for photocatalytic application in recent years [1-3]. However, irradiation with ultraviolet (UV) light to the surface of the catalyst reduces the efficiency due to its wide band energy (3.0-3.6 eV) [4]. To increase solar absorption efficiency, the use of narrowband semiconductors has been a topic of interest in recent studies [5,6]. Among these semiconductors, p-type copper oxide has emerged as promising material for photocatalysts due to its fascinating properties, such as small band gap (1.9-2.1 eV), and absorbing of solar radiation 300-620 nm, which covers 50% of photons of visible light [7]. In addition, Cu_2O is a non-toxic, environmentally friendly, earth abundant material, with low fabrication cost [8]. Moreover, the Cu/Cu_2O heterojunction can increase the photocatalytic properties of Cu_2O-based semiconductors because Cu can reduce the recombination of electron-hole pairs while transferring the photoelectrons [9-11].

Controlling the synthesis process of metal oxide nanoparticles is an important factor to be able to put the product into practical application. A small change in the lattice constant leads to a change in the band gap of the materials [12-14]. Many methods are reported for Cu_2O synthesis, including hydrothermal method, electro-deposition method, colloidal solution method, and thermal oxidation method [15-18]. Among these, colloidal solution synthesis is widely used because of its simple operation, low energy input, high productivity and quality, without any sophisticated, high-end equipment requirement, which can provide a greater degree of control [19,20]. The studies show that the change in the size and shape of the crystal led to the modification of the lattice constant and band gap of the material, which plays an important role in solar energy conversion efficiency [21,22]. In view of the above reasons, we are interested in studying the lattice modification of Cu/Cu_2O PNCs synthesized in colloidal solution.

XRD is a rapid analytical technique primarily used for phase identification and structural properties of a crystalline material. The advantages of this technique are simple and fast sample preparation, easy operation, rapid measurement, analysis of phases in the same sample, and direct determination of crystal structures [23]. Some structural parameters, such as lattice parameters, crystallite size, lattice strain and dislocation, are analyzed by using XRD method [24]. Usually, the perfect crystal will grow in all directions. However, due to their finite size, crystals will grow imperfectly, so that the crystal imperfections produce elongated and extended peaks in the XRD pattern [25]. The XRD database gives information about the main parameters, such as crystal size and lattice strain. Previous reports used some models to fit the database of XRD in order to obtain the precise values, such as the Nelson-Riley function and the Williamson-Hall method [25,26].

In this study, the crystallite size of the Cu/Cu_2O PNCs was calculated using the Scherrer equation and the lattice constant was estimated according to Bragg's law. Furthermore, the lattice constant was also calculated by using Nelson-Riley analysis. Other structural parameters such as dislocation, lattice strain were calculated using Williamson-Hall method (W-H) with XRD database. Based on the XRD database the Rietveld refinement method was also used to refine the quantitation, crystal structure, texture, and strain of Cu/

†To whom correspondence should be addressed.
E-mail: tamnguyentn@ynu.ac.kr, jhjung@ynu.ac.kr

Cu_2O PNCs.

EXPERIMENT

1. Materials and Methods

Copper sulfate pentahydrate ($CuSO_4 \cdot 5H_2O$, >99%) was used as a copper precursor, polyethylene glycol (MW 6,000) as a capping agent and size controller, L-ascorbic acid ($C_6H_8O_6$, >99%) as a protective agent to prevent the oxidation of nascent nanoparticles in synthesis process, sodium hydroxide (NaOH, >97%) as a pH controller, and sodium borohydride ($NaBH_4$, >95%) as a reducing agent. All chemicals were purchased from Sigma Aldrich and used without further purification. All chemicals were diluted in deionized (DI) water.

2. Synthesis of Cu/Cu_2O PNCs

In this synthesis, first, light blue solution was prepared by using 0.637 g $CuSO_4 \cdot 5H_2O$ dissolved in 25 mL DI water. Then, 0.25 g PEG was completely dissolved in 25 mL DI water and mixed with the precursor solution. Next, 0.102 g NaOH was dissolved in 25 mL DI water and added slowly into the previous solution;, the solution was stirred for 15 min. Then 0.025 mmol $C_6H_8O_6$ was added dropwise to the stirred solution and kept for 30 min. Finally, $NaBH_4$ was added in different concentrations (0.0, 1.0, 3.0, 5.0, 10.0 mol/L), which were coded as B0, B1, B3, B5, and B10. All the experiments were at 40 °C and 250 rpm during the whole process. The solutions were centrifuged at 5,000 rpm for 20 min, and washed three times by DI water and ethanol. The precipitate was collected and dried at 95 °C for 2 h. The synthesized powders were used for further characterization. This procedure is summarized in Fig. 1.

3. Materials Characterization

X-ray diffraction technique (PANalytical X' pert PRO) was used to measure the phase, crystallite size and lattice parameter of Cu/Cu_2O PNCs. Measurements are made with an incident beam of wavelength=1.5406 Å and the distance from the sample to the detector is adjusted within the angle range of 10-80° (2θ). The crystallite size and lattice constant were calculated by Scherrer equation (Eq. (1)) and Bragg's Law (Eq. (2)), respectively.

$$D = \frac{K\lambda}{\beta \cdot \cos\theta} \quad (1)$$

$$d_{hkl} = \frac{\lambda}{2\sin\theta} \quad (2)$$

where D is the average crystallite size, K is the Scherrer constant, λ is the X-ray wavelength (CuK_α=1.5406 Å), β is the line broadening at full width at half maximum (FWHM) in radians, d_{hkl} is the interplanar spacing in Å and θ is the Bragg's angle in degrees.

The mass fraction of Cu in the Cu/Cu_2O PNCs was calculated by Eq. (3) [27]:

$$Cu\ (\%) = \frac{C_{Cu\,(1\,1\,1)}}{C_{Cu\,(1\,1\,1)} + C_{Cu_2O\,(1\,1\,1)}} \quad (3)$$

where $C_{Cu(1\,1\,1)}$ and $C_{Cu_2O(1\,1\,1)}$ are the maximum count of peak (1 1 1) of Cu and Cu_2O in the XRD spectra, respectively. The mass percent of Cu_2O in Cu/Cu_2O PNCs is calculated similarly to Eq. (3) with the numerical element being $C_{Cu_2O(1\,1\,1)}$.

Rietveld refinement analysis method was used to filter lattice parameters through the d-value and to estimate the actual intensity of a particular phase or plane theoretically. From that, the accurate crystallite size, lattice parameter, strain, crystallinity, and quantitative analysis were obtained. The XRD databases were collected, integrated, calibrated and refined to the standard using the MAUD program.

RESULTS- DISCUSSION

1. Mechanism of Cu/Cu_2O PNC Formation

The reactions took place in the aqueous solution as:

$$CuSO_4 \rightarrow Cu^{2+} + SO_4^{2-} \quad (4)$$

$$Cu^{2+} + PEG \rightarrow [Cu.PEG]^{2+} \quad (5)$$

$$[Cu.PEG]^{2+} + 2OH^- \rightarrow Cu(OH)_2\downarrow \quad (6)$$

$$2Cu(OH)_2\downarrow + C_6H_8O_6 \rightarrow Cu_2O\downarrow + C_6H_6O_6 + 3H_2O \quad (7)$$

$$Cu_2O + C_6H_8O_6 \rightarrow Cu + C_6H_6O_6 + H_2O \quad (8)$$

$$4Cu^{2+} + BH_4^- + 8OH^- \rightarrow 4Cu + B(OH)_4 + 4H_2O \quad (9)$$

$$4Cu + O_2 \rightarrow 2Cu_2O\downarrow \quad (10)$$

The crystal formation in solution may be separated into four phases: (1) precursor formation, (2) nucleation, (3) growth, and (4) aging [20].

At first, the zero-charge molecules were dissolved in DI water and formed the ionic precursors which were formed with specific water content in order to allow nucleation to occur in the next

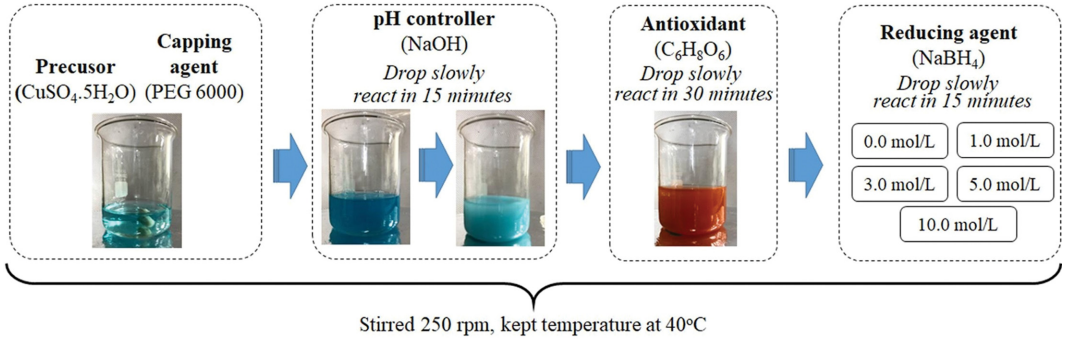

Fig. 1. General scheme of the Cu/Cu_2O composite experiment.

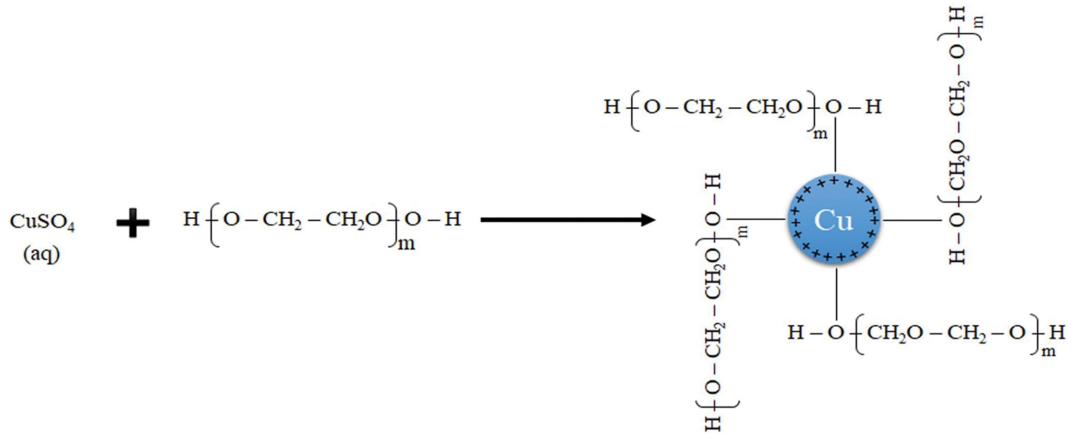

Fig. 2. Scheme of the interaction between the hydroxyl group of PEG and the surface positive charge of Cu^{2+} in solution $[Cu@PEG]^{2+}$.

stage (Eq. (4)). Nuclei tend to clump together after being formed to reduce the total surface energy. This aggregation is possibly a consequence of the van der Waals force among the nanocrystals; thus, it should be inhibited or restricted to limit the final grain size to the nanometer scale. The use of substances that lead to inter-individual repulsion is one of the best ways to solve the problem. PEG is exemplified for this type of aggregation and growth inhibitors [28]. When the Cu^{2+} ions were dispersed in the capping agent solution, the $[Cu@PEG]^{2+}$ ions were formed (Eq. (5)). PEG molecules can cover the Cu^{2+} surface by positive charge on the Cu^{2+} surface and the negative charge of the hydroxyl group of the PEG molecules (Fig. 2) [29].

Nucleation phase occurred when the sodium hydroxide was added into solution, the $[Cu@PEG]^{2+}$ reacted with OH^- and formed $Cu(OH)_2$ precipitate (Eq. (6)). At first, the solution turned from light blue to dark blue; as the OH^- solution was added continuously, it gradually changed to milky blue, indicating the $Cu(OH)_2$ formation. The growth phase occurs until the concentration of $Cu(OH)_2$ molecules reaches saturation. $Cu(OH)_2$ precipitate was reduced and formed Cu_2O nanoparticles after the addition of L-ascorbic acid (Eq. (7)). However, the excess amount of $C_6H_8O_6$ can further reduce

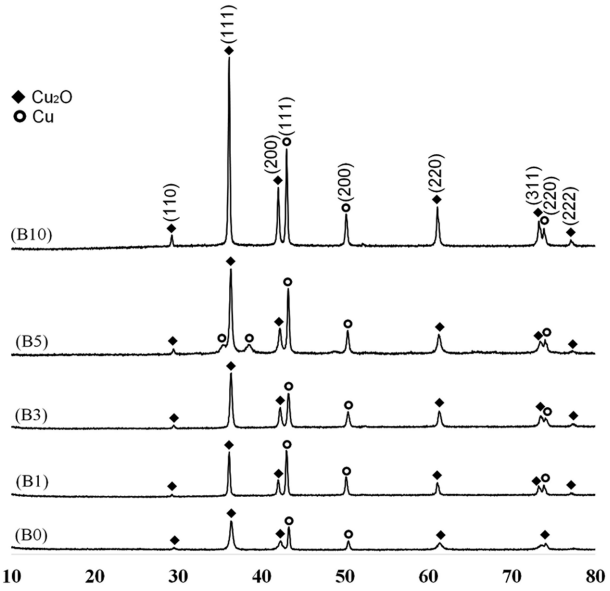

Fig. 3. XRD spectra of Cu/Cu_2O PNCs in different oxidant agent concentrations.

Table 1. The crystal values of Cu/Cu_2O PNCs at different oxidant agent concentration

	B0	B1	B3	B5	B10
a=b=c (Å)	4.26	4.267	4.258	4.258	4.26
$\alpha=\beta=\gamma$ (°)	90	90	90	90	90
Calculated density (g/cm^3)	6.15	6.12	6.15	6.15	6.15
Volume of cell ($10^6 \cdot pm^3$)	77.31	77.69	77.20	77.20	77.31
Crystallite size (nm)	245	372	473	481	587
Lattice parameter (Å)	4.056	4.076	4.073	4.070	4.060
Precised lattice constant (Å)	3.932	3.936	3.934	3.928	3.557
Lattice strain (%)	0.291	0.236	0.211	0.200	0.165
FWHM	0.536	0.348	0.350	0.429	0.815
Dislocation (δ)	1.77E-05	5.85E-06	8.79E-06	6.62E-06	3.81E-06
The mass fraction					
- Cu (%)	48.33	50.18	42.01	36.73	33.28
- Cu_2O (%)	51.67	49.82	57.99	63.27	66.72

the newly formed Cu_2O nanoparticles or only react on the surface of Cu_2O nanoparticles to form Cu or Cu/Cu_2O PNC, respectively. A brick red solution was obtained (Eq. (8)). After nucleation and growth phases, the average particle size may be changed in the aging phase. In this stage, the stirring speed determines the efficiency of the process, the aggregation may occur at a low speed.

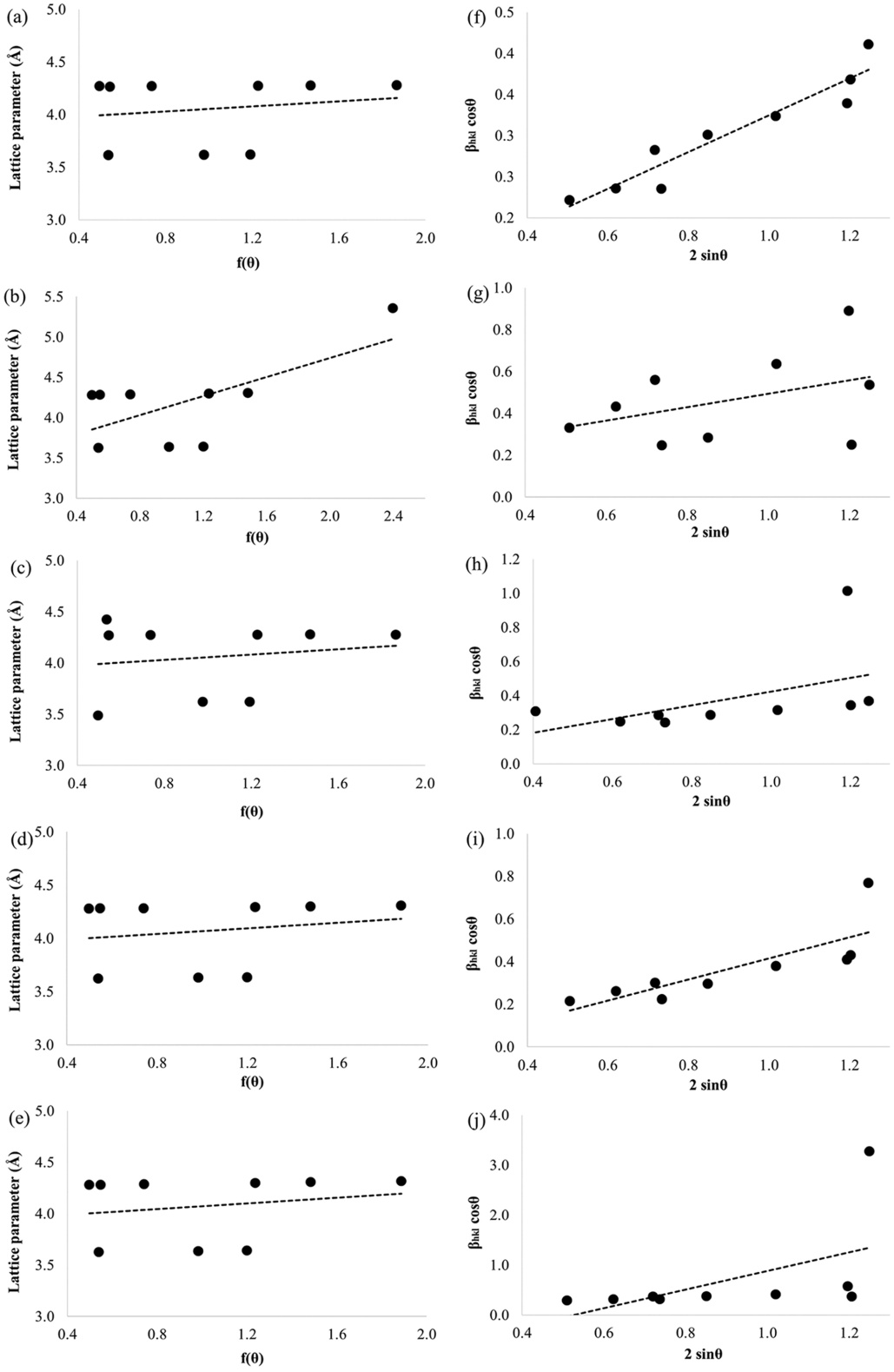

Fig. 4. The linear regression analysis between the lattice parameter and the Nelson-Riley function (a) B0, (b) B1, (c) B3, (d) B5, (e) B10; and Williamson-Hall method (f) B0, (g) B1, (h) B3, (i) B5, (j) B10.

With high stirring speed, the probability and energy of collision between particles will increase, leading to mechanical erosion [30]. With the addition of BH_4^-, the remaining Cu^{2+} ions are reduced to form Cu (Eq. (9)). However, the experiment was conducted under ambient temperature, the oxygen in the atmosphere was dissolved into the solution through the stirring process, and thus a part of Cu was oxidized and formed Cu_2O (Eq. (10)). As a result, the Cu/Cu_2O PNCs were obtained.

2. Powder X-ray Diffraction

The XRD patterns of as synthesized Cu/Cu_2O PNCs are shown in Fig. 3. The comparison of the position of the peaks with ICDD files No. 01-078-2076 and No. 785-1326 reveals that the crystal systems of Cu/Cu_2O PNCs are cubic with Pn-3m and Fm-3m space group, respectively. As shown in Fig. 3, three strong peaks at 43.18°, 50.36° and 74.04° of Cu metal (ICDD #785-1326) were observed corresponding to the planes (1 1 1), (2 0 0), (2 2 0) and the diffraction peaks at 29.23°, 36.10°, 41.98°, 61.08°, 73.53°, and 77.09° are attributed to the planes (1 1 0), (1 1 1), (2 0 0), (2 2 0), (3 1 1), and (2 2 2) of Cu_2O (ICDD #01-078-2076). These obtained results are well matched with previous reports [27,31-34]. The significantly enlarged peaks (FWHM) suggest that the material is composed of very small crystals (Table 1).

The bond length in the lattice was calculated using Bragg's Law (Eq. (2)) and the crystallite size was calculated using the Scherrer formula (Eq. (1)). It is obvious that for all diffraction peaks, when the BH_4^- concentration is increased, all the intensity of diffraction peaks will also increase. The increase in the electron density of the reflection planes is a possible reason for higher intensity of diffraction peaks. Moreover, the results of the calculated crystallite sizes in Table 1 also demonstrate the reason for the increase in the intensity of the peaks.

Due to the change of oxidant agent concentration, the lattice constant of crystal will be affected and different from the standard. Therefore, the precise values of the lattice parameters were estimated using the Nelson-Riley method (Eq. (11)):

$$f(\theta)=\frac{1}{2}\left(\frac{\cos^2\theta}{\sin\theta}+\frac{\cos^2\theta}{\theta}\right) \tag{11}$$

The precise lattice parameter of Cu/Cu_2O PNCs was calculated with the support of linear regression analysis between the lattice parameter and the Nelson-Riley function [35-37]. Fig. 4(a)-(e) shows the typical Nelson-Riley plots and parameters for Cu/Cu_2O PNCs at different oxidant agent concentrations. Table 1 shows that the precise lattice constant from Nelson-Riley function was estimated as 3.923 Å, 3.936 Å, 3.934 Å, 3.928 Å, and 3.557 Å for B0, B1, B3, B5, and B10, respectively. Compared to the lattice parameter of Cu/Cu_2O PNCs in Table 1, which is obtained from the ICDD, the precise lattice parameters were shorter. Additionally, the results show that the lattice constant decreases with increasing concentration of the oxidant agent.

The precise lattice parameters of PNCs were lower than those previously reported for Cu_2O due to the combination of Cu and Cu_2O [37,38]. To investigate the crystal structure of Cu/Cu_2O PNCs, the VESTA software was utilized to draw the combination between the Pn-3m and Fm-3m space groups of Cu_2O and Cu, respectively. As discussed above, due to the oxidation process, Cu and Cu_2O will be formed on the surface of the nanoparticles to create PNCs. Fig. 5 shows the crystal structure of the B0 PNC based on the precise lattice constant calculated from the Nelson-Riley function. The structures of the others have a similar structure with varying distance between atoms.

Lattice strain is used to consider the distribution of lattice parameters, such as dislocations, arising from crystal imperfection, deformity. The Williamson and Smallman's equation was used to calculate the dislocation density (δ) (Eq. (12)) [39,40].

$$\delta=\frac{1}{D^2} \tag{12}$$

where D is the crystallite size (nm) obtained from Eq. (1). In this formula, the line/volume dislocation is at lower position with better crystallinity at bigger particle size. Based on this calculation, it is known that the dislocation density of PNCs in this study was quite small. Here, the dislocation density for the dominant plane (1 1 1) decreased from 0.0000088 to 0.0000056 when the oxidant agent concentration increased. Small values of dislocation density indicate that the Cu/Cu_2O PNCs had a high degree of crystallin-

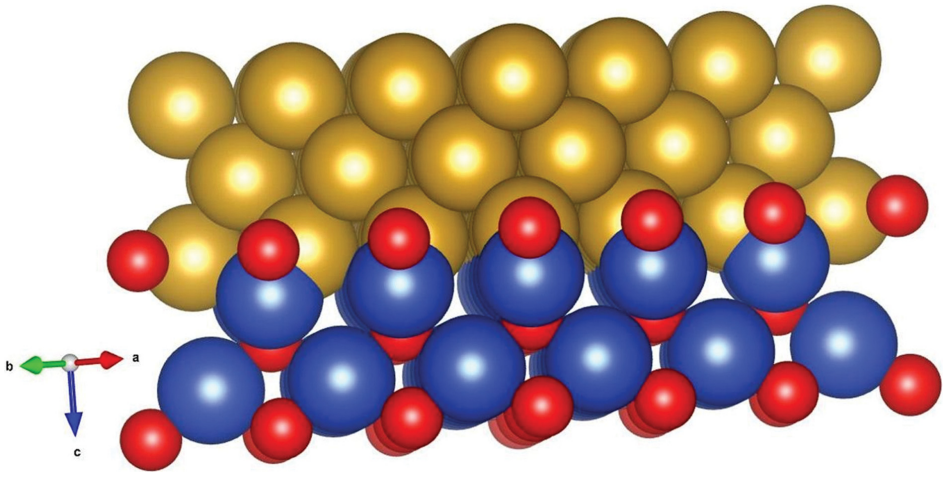

Fig. 5. The suggested crystal heterostructure diagram of Cu/Cu_2O PNC. The Cu1, O1 and Cu2 are yellow, red and blue dots, respectively.

ity [41].

The induced lattice strain of Cu/Cu_2O PNCs could be calculated by Williamson-Hall methods. Using the linear plot between $2\sin\theta$ and $\beta_{hkl}\cos\theta$, the lattice strain and crystallite size of Cu/Cu_2O PNCs may be calculated according to the slope and intercept of the linear equation (Fig. 4(f)-(j)) [25]. According to the model results, the lattice strains of Cu/Cu_2O PNCs from the slope of Williamson-Hall linear equation are 0.8559, 0.4954, 0.4032, 0.3208, and 0.2234 corresponding to B0, B1, B3, B5, and B10. This result shows that the lattice strain from the Williamson-Hall calculation is higher

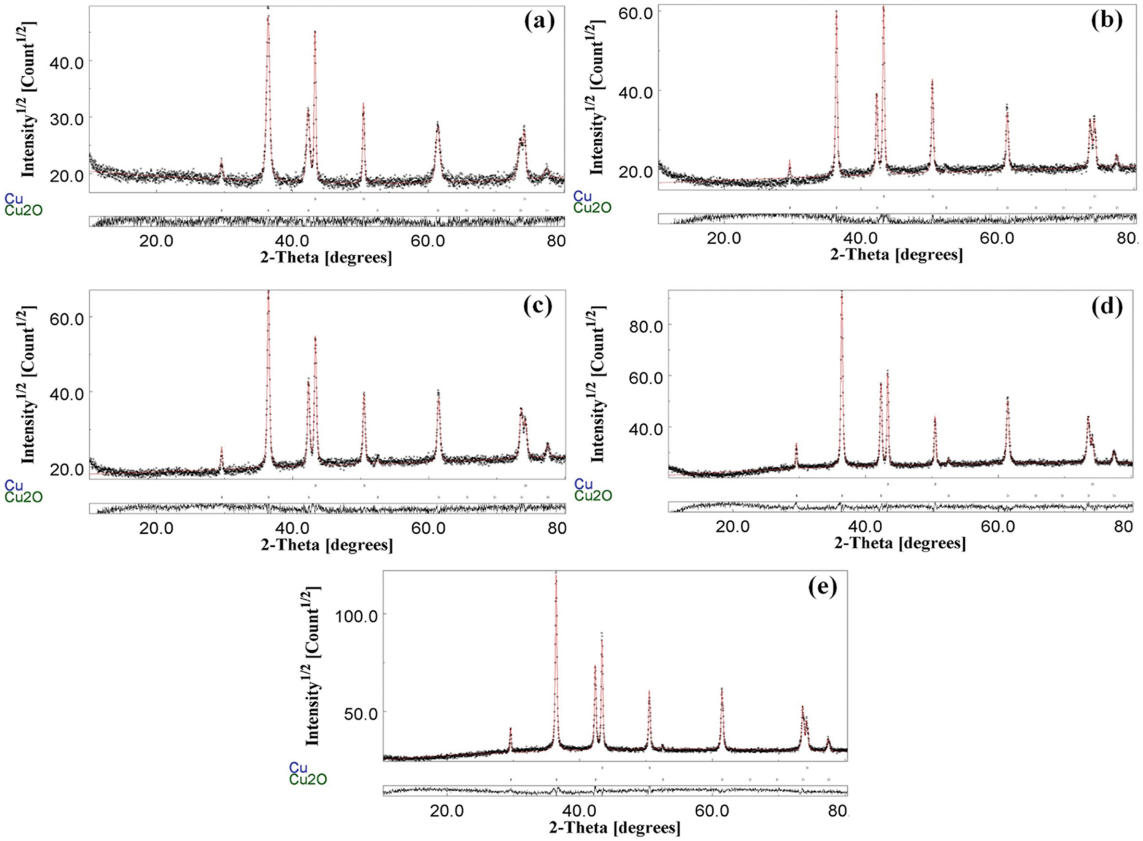

Fig. 6. The Rietveld refinement of (a) B0, (b) B1, (c) B3, (d) B5, and (e) B10. The difference between the XRD patterns (black-line) with Cu and Cu_2O.

Table 2. Rietveld refinement data on the reflection and atomic site of Cu/Cu_2O PNCs

					B0	B1	B3	B5	B10
Reflection list	h	k	l	Multiplicity	Microstrain (%)				
	1	1	0	12	3.0183	3.0184	3.0176	3.0171	3.0160
	1	1	1	8	2.4644	2.4645	2.4638	2.4635	2.4626
	2	0	0	6	2.1343	2.1343	2.1337	2.1334	2.1326
	1	1	1	8	2.0871	2.0868	2.0866	2.0863	2.0854
	2	0	0	6	1.8075	1.8072	1.8071	1.8068	1.8060
	2	2	0	12	1.5092	1.5092	1.5088	1.5086	1.5080
	3	1	1	24	1.2870	1.2870	1.2867	1.2865	1.2860
	2	2	0	12	1.2781	1.2779	1.2778	1.2776	1.2770
	2	2	2	8	1.2322	1.2323	1.2319	1.2317	1.2313
Atomic site list	Rietveld parameter				Cu1 - O1 - Cu2				
	x=y=z				0 - 0 - 0.25	0 - 0 - 0.25	0 - 0 - 0.25	0 - 0 - 0.25	0 - 0 - 0.25
	Multiplicity				4 - 2 - 4	4 - 2 - 4	4 - 2 - 4	4 - 2 - 4	4 - 2 - 4
	B neutro				0.736 - 0.799 - 0.668	0.272 - 0.157 - 0.032	0.455 - 0.700 - 0.088	0.463 - 0.043 - 0.696	0.282 - 0.912 - 1.774
	Sof.				1 - 1 - 1	1 - 1 - 1	1 - 1 - 1	1 - 1 - 1	1 - 1 - 1

than the lattice strain of Scherrer equation, as shown in Table 1. Additionally, the crystallite size of Cu/Cu_2O PNCs is also bigger than that of Bragg's Law calculation. The crystallite size of B0, B1, B3, B5 and B10 PNCs was obtained from the intercept point as 101, 173, 208, (-307) and (-374) nm, which are smaller than that of the calculation results, as shown in Table 1. Herein, B5 and B10 have negative intercept values, indicating shrinkage of the crystal [25].

To determine the exact composition of the material based on the XRD patterns, Rietveld refinement was conducted using the XRD experimental database of Cu/Cu_2O PNCs, as shown in Fig. 6. Necessary calculations, including scanning the XRD database with standard spectra of Cu_2O (COD ID 1000063, space group Pn-3m) and Cu (COD ID 5000216, space group Fm-3m), were performed on MAUD software. Good refinement for quantitative analysis, crystal structure analysis, textual analysis and strain analysis was obtained, both in Cu_2O and Cu. All nine intensity peaks of XRD patterns have been indicated and fixed with the reflection of Cu and Cu_2O. Fig. 6 shows that only the Cu and Cu_2O crystalline phases are stably present in samples. By Rietveld refinement using the MAUD program, the reflection and atomic site were calculated and shown in Table 2. The microstrains of each plane among PNCs are not significantly different, but a decreasing trend can be observed with increasing oxidant agent concentration and the main Bragg's reflection of Cu/Cu_2O PNCs attributed to the plane (3 1 1) peak (average is 1.2867%).

CONCLUSION

Cu/Cu_2O PNCs were synthesized by a simple colloidal solution method. By changing the oxidant agent concentration, we obtained diminutive changes of crystallite size and lattice parameters. The structural properties of PNCs were determined by XRD technique. XRD patterns revealed that the PNCs have cubic structure with the space group Pn-3m (Cu_2O) and Fm-3m (Cu).

The increasing oxidant agent concentration affected the intensity of XRD peaks. The calculation by the Nelson-Riley function proved that the precise lattice constants were higher than calculated by Bragg's Law. The calculated crystallite size from Williamson-Hall methods was smaller than that from the Scherrer formula. The lattice strain was also confirmed by using Williamson-Hall methods based on the XRD database. Additionally, Rietveld refinement was conducted to scan the experimental XRD patterns with the standards. From that refinement, we conclude that the microstrain of the crystal decreased with increasing concentration of the oxidant agent.

ACKNOWLEDGEMENTS

This work was supported by the Human Resources Program in Energy Technology of the Korea Institute of Energy Technology Evaluation and Planning (KETEP), granted financial resources from the Ministry of Trade, Industry & Energy, Republic of Korea. (No. 20204010600100).

REFERENCES

1. T. Bak, J. Nowotny, N. J. Sucher and E. D. Wachsman, *Adv. Appl. Ceram*., **111**, 4 (2012).
2. M. M. M. Melo, E. M. R. Rocha and E. L. Silva, *Manag. Environ. Qual*., **28**, 65 (2018).
3. A. M. Al-Hamdi, U. Rinner and M. Sillanpaa, *Process. Saf. Environ. Prot*., **107**, 190 (2017).
4. C. A. Gueymard, *Sol Energy*, **76**, 423 (2004).
5. J. Li, X. Liu, Z. Sun and L. Pan, *J. Colloid Interface Sci*., **463**, 145 (2016).
6. B. Liu, X. Liu, M. Ni, C. Feng, X. Lei, C. Li, Y. Gong, L. Niu, J. Li and L. Pan, *B. Appl. Surf. Sci*., **453**, 280 (2018).
7. J. Luo, L. Steier, M. K. Son, M. Schreier, M. T. Mayer and M. Graatzel, *Nano Letters*, **16**, 1848 (2016).
8. I. V. Bagal, N. R. Chodankar, M. A. Hassan, A. Waseem, M. A. Johar, D. H. Kim and S. W. Ryu, *Int. J. Hydrogen Energy*, **44**, 21351 (2019).
9. L. Xu, C. Srinivasakannan, J. Peng, M. Yan, D. Zhang and L. Zhang, *Appl. Surf. Sci*., **331**, 449 (2015).
10. B. Zhou, Z. Liu, H. Wang, Y. Yang and W. Su, *Catal. Lett*., **132**, 75 (2009).
11. T. Kou, Y. Wang, C. Zhang, J. Sun and Z. Zhang, *Chem. Eng. J*., **223**, 76 (2013).
12. H. Cao, S. Huang, Y. Yu, Y. Yan, Y. Lu and Y. Cao, *J. Colloid Interface Sci*., **486**, 176 (2017).
13. M. R. D. Khaki, M. S. Shafeeyan, A. A. A. Raman and W. M. A. W. Daud, *J. Mol. Liq*., **258**, 354 (2018).
14. S. Chen, F. Liu, M. Xu, J. Yan, F. Zhang, W. Zhao, Z. Zhang, Z. Deng, J. Yun, R. Chen and C. Liu, *J. Colloid Interface Sci*., **553**, 613 (2019).
15. B. Yuan, X. Liu, H. Fu, J. Liu, Q. Zhu and M. Wu, *Sol Energy*, **188**, 265 (2019).
16. B. Wang, Y. Xie, T. Yang, L. Wang, L. Wang and D. Jin, *Surf. Eng*., **36**, 199 (2020).
17. S. Behjati, S. Sheibani, J. Herritsch and J. M. Gottfried, *Mater. Res. Bull*., **130**, 110920 (2020).
18. C. Xu, K. V. Manukyan, R. A. Adams, V. G. Pol, P. Chen and A. Varma, *Carbon*, **142**, 51 (2019).
19. A. Ahmed, N. S. Gajbhiye and A. G. Joshi, *Mater. Chem. Phys*., **129**, 740 (2011).
20. G. Oskam, *J. Sol Gel Sci. Technol*., **37**, 161 (2006).
21. D. L. Ferreira, J. C. L. Sousa, R. N. Maronesi, J. Bettini, M. A. Schiavon, A. V. Teixeira and A. G. Silva, *J. Chem. Phys*., **147**, 154102 (2017).
22. Y. Shi, J. Lian, W. Hu, Y. Liu, G. He, K. Jin, H. Song, K. Dai and J. Fang, *J. Alloys Compd*., **788**, 891 (2019).
23. G. Taglieri, C. Mondelli, V. Daniele, E. Pusceddu and A. Trapananti, *AMPC*, **3**, 108 (2013).
24. A. Chauhan and P. Chauhan, *J. Anal. Bioanal. Tech*., **5**, 1 (2014).
25. P. C. Dey, S. Sarkar and R. Das, *Mater. Sci. Pol*., **38**, 271 (2020).
26. S. G Pandya, J. P. Corbett, W. M. Jadwisienczak and M. E. Kordesch, *Phys. E: Low-Dimens. Syst. Nanostructures*, **79**, 98 (2016).
27. B. Kumar, S. Saha, K. Ojha and A. K. Ganguli, *Mater. Res. Bull*., **64**, 283 (2015).
28. T. M. D. Dang, T. T. T. Le, E. F. Blanc and M. C. Dang, *Adv. Nat. Sci: Nanosci. Nanotechnol*., **2**, 015009 (2011).
29. K. Shameli, M. B. Ahmad, A. Zamanian, P. Sangpour, P. Shabanzadeh, Y. Abdollahi and M. Zargar, *Int. J. Nanomedicine*, **7**, 5603 (2012).

30. Y. Bai, T. Yang, Q. Gu, G. Cheng and R. Zheng, *Powder Technol.*, **227**, 35 (2012).
31. L. Xiong, H. Xiao, S. Chen, Z. Chen, X. Yi, S. Wen, G. Zheng, Y. Ding and H. Yu, *RSC Adv.*, **4**, 62115 (2014).
32. M. Eslami, F. Golestani-fard, H. Saghafian and A. Robin, *Mater. Des.*, **58**, 557 (2014).
33. Y. Dong, K. Wang, Y. Tan, Q. Wang, J. Li, H. Mark and S. Zhang, *Nanoscale Res. Lett.*, **13**, 1 (2018).
34. Q. He, Y. Tian, Y. Wu, J. Liu, G. Li, P. Deng and D. Chen, *Biomolecules*, **9**, 176 (2019).
35. J. P. K. Chintala, S. D. Kaushik, M. C. Varma, G. S. V. R. K. Choudary and K. H. Rao, *J. Supercond. Nov. Magn.*, **34**, 149 (2021).
36. N. Khemiri, D. Abdelkader, B. Khalfallah and M. Kanzari, *OJSTA*, **2**, 33 (2013).
37. M. Mallik, S. Monia, M. Gupta, A. Ghosh, M. P. Toppo and H. Roy, *J. Alloys Compd.*, **829**, 154623 (2020).
38. A. A. Akl, S. A. Mahmoud, S. M. Al-Shomar and A. S. Hassanien, *Mater. Sci. Semicond. Process.*, **74**, 183 (2018).
39. S. A. A. Terohid, S. Heidari, A. Jafari and S. Asgary, *Appl. Phys. A*, **124**, 1 (2018).
40. W. Shim, J. Ham, K. I. Lee, W. Y. Jeung, M. Johnson and W. Lee, *Nano Lett.*, **9**, 18 (2009).
41. I. W. Sutapa, A. W. Wahab, P. Taba and N. L. Nafie, *J. Phys. Conf. Ser.*, **979**, 012021 (2018).